Properties and Structures of RE_2O_3−Al_2O_3−SiO_2 (RE = Y, Lu) Glasses Probed by Molecular Dynamics Simulations and Solid-State NMR: The Roles of Aluminum and Rare-Earth Ions for Dictating the Microhardness

Shahriar Iftekhar,[†] Bholanath Pahari,[†] Kirill Okhotnikov,[†] Aleksander Jaworski,[†] Baltzar Stevensson,[†] Jekabs Grins,[‡] and Mattias Edén[†,*]

[†]Physical Chemistry Division and [‡]Inorganic and Structural Chemistry Division, Department of Materials and Environmental Chemistry, Arrhenius Laboratory, Stockholm University, SE-106 91 Stockholm, Sweden

Ⓢ *Supporting Information*

ABSTRACT: By combining molecular dynamics (MD) simulations with ^{29}Si and ^{27}Al magic-angle spinning nuclear magnetic resonance (NMR) spectroscopy, we present a comprehensive structural report on rare-earth (RE) aluminosilicate (AS) glasses of the RE_2O_3−Al_2O_3−SiO_2 (RE = Y, Lu) systems, where the latter is studied for the first time. The structural variations stemming from changes in the glass composition within each RE system—as well as the effects of the increased cation field-strength (CFS) of Lu^{3+} relative to Y^{3+}—are explored and correlated to measured physical properties, such as density, molar volume, glass transition temperature, and Vickers hardness (H_V). ^{29}Si NMR reveals a pronounced network ordering for an increase in either the RE or Al content of the glass. Al mainly assumes tetrahedral coordination, but significant AlO_5 and AlO_6 populations are present in all structures, with elevated amounts in the Lu-bearing glasses compared to their Y analogues. The MD-derived oxygen speciation comprises up to 3% of free O^{2-} ions, as well as non-negligible amounts (4−19%) of $O^{[3]}$ coordinations ("oxygen triclusters"). While the SiO_4 groups mainly accommodate the nonbridging oxygen ions, a significant fraction thereof is located at the AlO_4 tetrahedra, in contrast to the scenario of analogous alkali- and alkaline-earth metal-based AS glasses. The average coordination numbers (CNs) of Al and RE progressively increase for decreasing Si content of the glass, with the average CN of the RE^{3+} ions depending linearly on both the amount of Si and the fraction of AlO_5 groups in the structure. The Vickers hardness correlates strongly with the average CN of Al, in turn dictated by the CFS and content of the RE^{3+} ions. This is to our knowledge the first structural rationalization of the well-known compositional dependence of H_V in RE bearing AS glasses.
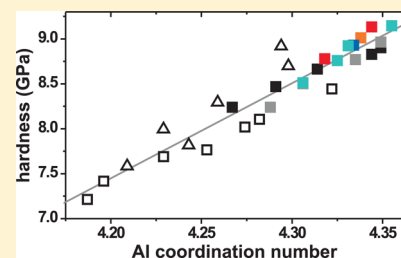
1. INTRODUCTION

Thanks to their high glass transition temperatures (T_g) and beneficial mechanical and optical properties, such as high Vickers hardness (H_V), Young's modulus and refractive index, combined with excellent corrosion resistance, rare earth (RE) aluminosilicate (AS) glasses of the ternary RE_2O_3−Al_2O_3−SiO_2 systems[1−8] constitute host materials in a multitude of optical devices and are suggested for radioactive waste-storage.[9] Microspheric Y AS glasses are used in radiotherapy for *in situ* cancer treatment,[3,10,11] while the Y_2O_3−Al_2O_3 sister system manifests an unusual density-driven amorphous phase separation.[12−15] Despite that the favorable physical properties of RE AS glasses derive from their structural features, the latter are relatively sparsely investigated and poorly understood. Many RE AS properties enhance for increasing RE^{3+} cation field strength (CFS), given by z/r^2 with z and r denoting the charge and radius of the cation, respectively. The present study elucidates composition/property/structure correlations of RE−Al−Si−O glasses where RE represents Y or Lu. The Y^{3+} and Lu^{3+} cations exhibit similar Shannon-Prewitt ionic radii[16] of 0.90 and 0.86 Å, respectively (assuming octahedral coordina-

tions). Hence, AS glasses based on these ions are expected to display similar properties and structures. Yet, while Y AS glasses are hitherto the most explored among all RE counterparts, studies of the Lu_2O_3−Al_2O_3−SiO_2 system are very limited.[7,17]

The network of an AS glass is built by interconnected $Q_{Si}^n(mAl)$ and $Q_{Al}^n(mSi)$ tetrahedra, where the subscript specifies the central cation that accommodates $4-n$ non-bridging oxygen (NBO) ions, and being linked to n neighboring Al^{3+}/Si^{4+} cations through bridging oxygen (BO) atoms. Out of these n linkages, there are m **Si**−O−Al and m **Al**−O−Si bonds at each $Q_{Si}^n(mAl)$ and $Q_{Al}^n(mSi)$ moiety, respectively, implying $n-m$ homoatomic T−O−T bridges. Owing to an additional negative charge associated with the $[AlO_4]^-$ groups, $Al^{[4]}$−O−$Al^{[4]}$ linkages are essentially absent (the "Loewenstein Al avoidance principle"[18])—as are NBO-bearing AlO_4 tetrahedra—in AS glasses based on alkali and alkaline-earth metals (except for Mg^{2+}) and associated with

molar ratios $n_{Al}/n_{Si} \leq 1$.[19−22] However, *both* these features are expected to gradually relax as the CFS of the modifier ion increases,[21−30] and some evidence exists for $Q_{Al}^n(mSi) \rightarrow Q_{Al}^{n-1}(mSi)$ depolymerizations even in Ca AS glasses.[27,28,31] Consequently, for RE-based AS glasses, the high charge of the trivalent RE^{3+} cations may randomize the partitioning of the NBO ions among the tetrahedral network species. In a previous ^{29}Si NMR study of the La−Al−Si−O system,[29] we concluded that both the intermixing of AlO_4/SiO_4 tetrahedra in the glass network and their BO/NBO distribution are significantly disordered. Such structural aspects will here be assessed more quantitatively by exploiting molecular dynamics (MD) simulations as a probe for AS glasses incorporating Y^{3+} and Lu^{3+} ions. MD investigations of RE AS glasses are sparse and have hitherto only been considered for members of the Y_2O_3−Al_2O_3−SiO_2 system: Du[32] reported data from glasses featuring low SiO_2-contents, whereas Christie and Tilocca[11] examined two compositions of relevance for *in situ* cancer treatment.

RE_2O_3−Al_2O_3−SiO_2 glasses also differ in other structural features relative to amorphous AS phases that incorporate lower-CFS mono- or divalent network modifiers. For instance, the former structures manifest significant contributions of AlO_5 polyhedra,[7,8,22,24,30,33−39] regardless if both conditions $n_{Al}/n_{Si} \leq 1$ and $n_{Al}/n_{RE} \leq 3$ are obeyed so that (formally) a local accumulation of negative charges may be avoided by ensuring a strict Si−O−Al[4] alternation in the network, as well as full charge-balance of all $Q_{Al}^n(mSi)$ groups by the RE^{3+} cations. The AlO_5 abundance is observed to increase as the RE^{3+} CFS enhances across the series La<Y<Lu<Sc.[7,8,24,36−38] By combining data from MD modeling with experimental [29]Si and [27]Al magic-angle spinning (MAS) nuclear magnetic resonance (NMR) spectroscopy, we investigate the relationship between the $Al^{[p]}$ (p = 4, 5, 6) speciation and the sample composition for 13 Y−Al−Si−O and 17 Lu−Al−Si−O glasses, the latter set covering the entire glass-forming region of the Lu_2O_3−Al_2O_3−SiO_2 system. Further, the speciations of $RE^{[p]}$ and $O^{[p]}$ coordinations are examined, revealing significant amounts (4−19%) of $O^{[3]}$ coordinations[19,40−44] and up to 3% of free O^{2-} ions ($O^{[0]}$) in the glass structures.

We also correlate the compositions of the RE AS glasses with their physical properties, such as the density (ρ), molar volume (M_V), compactness (C; ion packing density), T_g and H_V. The latter depends strongly on the RE^{3+}-dictated populations of AlO_5 and AlO_6 groups in the AS glass structure. The enhanced structural cross-linking of these higher-coordination polyhedra (as compared with AlO_4) is attributed as the main source of the well-known, but hitherto not fully explained, increase of H_V for growing CFS or content of the RE^{3+} ions in AS oxide and oxynitride glasses.[4−7,17,34,45,46]

2. MATERIALS AND METHODS

2.1. Glass Preparation and Characterization. The Lu and Y AS glasses were prepared in batches of 2.5 and 4.0 g, respectively, by using ball-milled mixtures of precalcined (at 300 °C) Lu_2O_3, Y_2O_3, Al_2O_3, and SiO_2 precursors (Chempure; 99.99% purity). 0.1 wt % of Gd_2O_3 was added to each batch to enhance the [29]Si spin−lattice relaxation for the NMR experimentation. The mixtures were heated in Pt crucibles in steps of 200 °C, with successive holding intervals of 0.5 h up to the final temperature of 1600 °C (for Y) or 1650 °C (for Lu), where each melt was held for 1 h (Y) or 2 h (Lu) and then quenched by immersing the bottom of the crucible in water. The losses during synthesis were generally <1.5 wt %.

Powder X-ray diffraction was performed on each specimen over a 2θ range of 10°−70° by using a Panalytical X'pert PRO MPD diffractometer and Cu $K\alpha_1$ radiation for 4 h per sample, giving a lower detection limit of $\lesssim 1\%$ for crystalline impurities. Samples marked by asterisks in Figure S1 of the Supporting Information comprise larger amounts of crystalline material.

Polished AS glasses were coated by a 10−20 nm thick carbon film and were examined by scanning electron microscopy (SEM) with a JEOL JSM 7000F microscope in backscatter electron imaging mode at 15 kV acceleration voltage. Besides identifying minor amounts (<5%) of poorly ordered SiO_2-rich impurity phases in some of the Lu-bearing samples, SEM revealed amorphous phase separation in a few specimens: they are depicted by shaded boxes in Figure S1 and were together with the partially crystallized specimens not considered further. All remaining samples constitute homogeneous glasses, as also confirmed by transmission electron microscopy studies on a selected set of specimens: phase-separation could be excluded down to a length-scale $\lesssim 10$ nm, i.e., within the limits of our instrumentation.

The physical-property measurements are only outlined briefly, as they followed the same procedures as described in detail in our previous work.[7,45] T_g-values were determined on powdered samples by differential thermal analysis with a heating rate of 40 °C/min up to 1350 °C in flowing air, by using a SETARAM Labsys instrument. Vickers hardness estimates (≥ 7 measurements with a 0.982 N load applied for 20 s) employed a Matsuzawa microhardness tester (MXT-α1) equipped with a pyramidal diamond indentor. The H_V-values were calculated by the procedure of Anstis et al.[47] Densities were obtained according to the Archimedes method in distilled water. They were used to determine M_V and C of each glass, whose molar mass $M = \sum_E x_E M_E$ was calculated from the atomic fractions x_E and molar masses M_E of the constituent elements E = (Y, Lu, Al, Si, O). The molar volume was obtained as $M_V = \rho/M$, with the compactness estimated according to $C = N_A/M_V \sum_E x_E V_E$, where N_A is Avogadro's constant and $V_E = 4\pi r_E^3/3$ the ion volume calculated from the Shannon−Prewitt ionic radius r_E.[16] The ion-species were assumed to exhibit coordination numbers $\{Z_{RE}, Z_{Al}, Z_{Si}, Z_O\}$ = {6, 4, 4, 2} throughout in all glasses; no significant changes of the C-values resulted if instead employing the NMR-derived fractional populations of AlO_4, AlO_5, and AlO_6 polyhedra (see section 3.4.1) in the calculations.

2.2. Sample Compositions and Notation. Each cation content was determined from an average over ten analyses of distinct glass fragments using SEM coupled to a LINK INCA (Oxford Instruments) energy-dispersive X-ray (EDX) detector. Tables 1 and 2 list the nominal and EDX-analyzed glass compositions. We denote each specimen by $RE_b^a(r)$, with RE representing Lu or Y, a and b the *nominal* n_{Al}/n_{Si} and n_{RE}/n_{Si} molar ratios of the *batch*, respectively, whereas r is defined by

$$r = \frac{n_O}{n_{Si} + n_{Al}} \qquad (1)$$

The nominal and EDX-analyzed compositions generally agreed within 98%, with the largest deviations ($\approx 4\%$ relative) observed for the RE contents of the $Y_{0.62}^{1.00}(2.21)$ and $Lu_{0.63}^{0.80}(2.30)$ specimens. This justifies our use of the nominal glass compositions listed in Tables 1 and 2; they are illustrated in Figure S1 (Supporting Information). Onward, x denotes a *fraction* of the relevant entity specified by a subscript; e.g., x_E

18395

dx.doi.org/10.1021/jp302672b | *J. Phys. Chem. C* 2012, 116, 18394−18406

Table 1. Y–Al–Si–O Glass Compositions, Physical Properties, and ^{29}Si NMR Parameters[a]

label	formula	n_{Al}/n_Y	aY_2O_3 (mol %)	bAl_2O_3 (mol %)	$cSiO_2$ (mol %)	T_g (°C)	ρ (gcm^{-3})	M_V (cm^{3}mol^{-1})	C	H_V (GPa)	$-\delta_{max}$ (ppm)	$-\delta_{CG}$ (ppm)	fwhm (ppm)
Y$^{0.55}_{0.40}$(2.21)	Y$_{0.40}$SiAl$_{0.55}$O$_{3.42}$	1.36	13.65(13.56)	18.50(18.67)	67.85(67.77)	893	3.13	7.94	0.518	7.30	91.3	92.9	22.0
Y$^{0.65}_{0.45}$(2.21)	Y$_{0.45}$SiAl$_{0.65}$O$_{3.64}$	1.44	14.50(14.94)	20.90(21.26)	64.60(63.80)	–	3.18	7.88	0.521	7.40	89.9	91.8	21.4
Y$^{0.80}_{0.52}$(2.21)	Y$_{0.52}$SiAl$_{0.80}$O$_{3.98}$	1.55	15.60(16.07)	24.12(24.48)	60.28(59.45)	897	3.27	7.74	0.530	7.78	87.5	89.6	18.8
Y$^{1.00}_{0.62}$(2.21)	Y$_{0.62}$SiAl$_{1.00}$O$_{4.43}$	1.63	17.05(16.93)	27.70(28.74)	55.25(54.33)	891	3.37	7.62	0.537	7.85	86.0	87.7	16.6
Y$^{1.17}_{0.69}$(2.21)	Y$_{0.69}$SiAl$_{1.17}$O$_{4.80}$	1.69	17.93(18.16)	30.31(30.62)	51.76(51.22)	895	3.42	7.56	0.540	8.11	84.8	86.8	15.5
Y$^{1.30}_{0.76}$(2.21)	Y$_{0.76}$SiAl$_{1.30}$O$_{5.09}$	1.71	18.70(18.70)	32.05(31.80)	49.25(49.50)	–	3.46	7.51	0.543	8.20	84.4	86.2	15.0
Y$^{1.80}_{1.02}$(2.21)[b]	Y$_{1.02}$SiAl$_{1.80}$O$_{6.23}$[b]	1.77[b]	21.16[b]	37.34[b]	41.50[b]	894	3.60	7.38	0.551	8.54	82.0	83.3	12.4
Y$^{0.40}_{0.56}$(2.45)	Y$_{0.56}$SiAl$_{0.40}$O$_{3.43}$	0.72	18.79(18.49)	13.54(13.89)	67.67(67.62)	–	3.40	7.83	0.532	7.67	87.3	90.0	20.2
Y$^{0.55}_{0.65}$(2.45)	Y$_{0.65}$SiAl$_{0.55}$O$_{3.80}$	0.84	20.36(20.74)	17.14(17.87)	62.50(61.39)	894	3.46	7.77	0.534	7.91	85.1	87.2	16.6
Y$^{0.65}_{0.72}$(2.45)	Y$_{0.72}$SiAl$_{0.65}$O$_{4.04}$	0.91	21.25(21.39)	19.27(19.82)	59.48(58.79)	–	3.51	7.74	0.536	8.09	84.4	86.6	16.0
Y$^{0.80}_{0.81}$(2.45)	Y$_{0.81}$SiAl$_{0.80}$O$_{4.41}$	0.99	22.39(21.82)	22.20(22.60)	55.41(55.58)	–	3.59	7.63	0.542	8.39	83.3	85.2	14.2
Y$^{1.00}_{0.94}$(2.45)	Y$_{0.94}$SiAl$_{1.00}$O$_{4.90}$	1.07	23.75(24.17)	25.43(25.99)	50.82(49.84)	897	3.64	7.60	0.543	8.80	82.5	84.2	12.8
Y$^{1.17}_{1.05}$(2.45)	Y$_{1.05}$SiAl$_{1.17}$O$_{5.33}$	1.12	24.79(24.74)	27.79(28.24)	47.42(47.02)	896	3.72	7.48	0.551	9.02	81.7	83.1	11.9

[a]Each specimen is labeled Y$^{n_{Al}/n_{Si}}_{n_Y/n_{Si}}$ (r), where n_E represents the stoichiometric coefficient of element E. The numbers {a, b, c} specify the nominally batched oxide equivalents of the $aY_2O_3–bAl_2O_3–cSiO_2$ composition. Values within parentheses correspond to EDX-analyzed oxide equivalents. δ_{max}, δ_{CG}, and fwhm denote the peak maximum, center-of gravity and the full width at half-maximum, respectively, of each ^{29}Si NMR peak. The uncertainties of the experimental data are as follows: T_g (±2 °C); ρ (±0.01 gcm^{-3}); M_V (±0.02 cm^{3}mol^{-1}); C (±0.001); H_V (±0.06 GPa); δ_{max} (±0.15 ppm); δ_{CG} (±0.25 ppm); fwhm (±0.2 ppm). [b]The EDX-analyzed composition was used for this specimen; the respective (a, b, c) coefficients of the nominal composition is (21.36, 39.32, 39.32) mol %.

Table 2. Lu–Al–Si–O Glass Compositions, Physical Properties and ^{29}Si NMR Parameters[a]

label	formula	n_{Al}/n_{Lu}	aLu_2O_3 (mol %)	bAl_2O_3 (mol %)	$cSiO_2$ (mol %)	T_g (°C)	ρ (g cm^{-3})	M_V (cm^{3}mol^{-1})	C	H_V (GPa)	$-\delta_{max}$ (ppm)	$-\delta_{CG}$ (ppm)	fwhm (ppm)
$Lu^{0.47}_{0.61}$(2.07)	$Lu_{0.61}SiAl_{1.47}O_{5.12}$	2.40	15.00(15.02)	36.00(35.99)	49.00(48.99)	910	4.24	7.38	0.546	9.11	–	–	–
$Lu^{1.27}_{0.58}$(2.10)	$Lu_{0.58}SiAl_{1.27}O_{4.77}$	2.20	15.00(15.03)	33.00(33.04)	52.00(51.93)	–	4.26	7.38	0.547	9.03	–	–	–
$Lu^{0.65}_{0.45}$(2.21)	$Lu_{0.45}SiAl_{0.65}O_{3.65}$	1.44	14.50(14.14)	20.97(20.68)	64.53(65.18)	911	4.13	7.69	0.532	8.33	89.1	90.9	22.0
$Lu^{0.80}_{0.52}$(2.21)	$Lu_{0.52}SiAl_{0.80}O_{3.98}$	1.55	15.60(15.17)	24.12(23.93)	60.28(60.90)	907	4.24	7.63	0.535	8.56	88.0	89.6	20.6
$Lu^{1.00}_{0.62}$(2.21)	$Lu_{0.62}SiAl_{1.00}O_{4.43}$	1.63	17.05(16.77)	27.70(27.63)	55.25(55.60)	905	4.40	7.55	0.539	8.76	85.4	87.3	17.9
$Lu^{1.17}_{0.69}$(2.21)	$Lu_{0.69}SiAl_{1.17}O_{4.80}$	1.69	17.93(17.77)	30.31(30.73)	51.76(51.50)	901	4.50	7.48	0.543	8.93	84.2	85.9	15.7
$Lu^{1.30}_{0.76}$(2.21)	$Lu_{0.76}SiAl_{1.30}O_{5.09}$	1.71	18.70(18.11)	32.05(31.96)	49.25(49.93)	902	4.52	7.54	0.538	9.00	83.9	85.5	15.5
$Lu^{0.65}_{0.55}$(2.30)	$Lu_{0.55}SiAl_{0.65}O_{3.80}$	1.18	17.20(17.43)	20.30(20.15)	62.50(62.42)	–	4.42	7.64	0.537	8.33	–	–	–
$Lu^{0.80}_{0.63}$(2.30)	$Lu_{0.63}SiAl_{0.80}O_{4.14}$	1.28	18.30(17.56)	23.37(23.46)	58.33(58.98)	–	4.51	7.62	0.537	8.60	–	–	–
$Lu^{1.00}_{0.74}$(2.30)	$Lu_{0.74}SiAl_{1.00}O_{4.62}$	1.35	19.80(19.25)	26.80(27.01)	53.40(53.74)	907	4.62	7.60	0.537	8.87	83.9	85.6	16.2
$Lu^{1.17}_{0.82}$(2.30)	$Lu_{0.82}SiAl_{1.17}O_{4.98}$	1.43	20.50(19.95)	29.30(29.48)	50.20(50.57)	–	4.75	7.46	0.546	9.07	–	–	–
$Lu^{0.65}_{0.62}$(2.37)	$Lu_{0.62}SiAl_{0.65}O_{3.91}$	1.04	19.04(18.78)	19.86(20.29)	61.10(60.93)	–	4.51	7.78	0.528	8.61	86.1	88.0	18.5
$Lu^{0.80}_{0.71}$(2.37)	$Lu_{0.71}SiAl_{0.80}O_{4.26}$	1.14	20.13(20.08)	22.87(23.22)	57.00(56.70)	–	4.62	7.72	0.531	8.86	–	–	–
$Lu^{1.00}_{0.83}$(2.37)	$Lu_{0.83}SiAl_{1.00}O_{4.74}$	1.21	21.60(21.21)	26.10(25.72)	52.30(53.07)	902	4.84	7.52	0.544	9.03	82.8	84.4	14.9
$Lu^{1.17}_{0.92}$(2.37)	$Lu_{0.92}SiAl_{1.17}O_{5.13}$	1.27	22.50(22.24)	28.55(28.72)	48.95(49.04)	–	4.84	7.61	0.536	9.25	–	–	–
$Lu^{0.80}_{0.81}$(2.45)	$Lu_{0.81}SiAl_{0.80}O_{4.41}$	0.99	22.38(22.56)	22.20(22.20)	55.42(55.24)	–	4.95	7.52	0.546	8.88	–	–	–
$Lu^{1.00}_{0.94}$(2.45)	$Lu_{0.94}SiAl_{1.00}O_{4.90}$	1.07	23.75(23.83)	25.43(25.83)	50.82(50.34)	908	5.05	7.50	0.546	9.24	81.7	83.8	14.1

[a]The content is analogous to that explained in the footnote of Table 1.

represents the molar fraction of element E out of the *cations*, i.e.,

$$x_E = n_E/(n_{Si} + n_{Al} + n_{RE}), \quad \text{with } E = Si, Al, \text{ or } RE \quad (2)$$

2.3. Solid-State NMR. ^{29}Si MAS NMR experiments were conducted at 9.4 T (79.5 MHz ^{29}Si Larmor frequency) with an Agilent/Varian/Chemagnetics Infinity−400 spectrometer, using glass powders filled in 6 mm zirconia rotors spinning at 8.00 kHz. The NMR spectra were recorded using 90° pulses at a nutation frequency of 37 kHz, 722−1712 accumulated signal transients and relaxation delays in the range of 150−360 s; the latter was selected for each sample from a separate saturation-recovery experiment to provide quantitative NMR spectra. ^{29}Si chemical shifts are quoted relative to neat tetramethylsilane (TMS).

^{27}Al MAS NMR experimentation was performed at 14.1 T (−156.4 MHz Larmor frequency) using a Bruker Avance-III spectrometer and 3.2 mm rotors spinning at 24.00 kHz. Short (≤0.3 μs) pulses were used at an rf nutation frequency of 100 kHz, calibrated on a 1 M Al^{3+}(aq) solution that also served for shift referencing. The spectral window was 600 kHz, the relaxation delays 3.0 s, and the number of accumulated transients ranged between 8000−12000.

No signal apodization was applied in the processing of the ^{27}Al NMR data, whereas that for ^{29}Si used 150−200 Hz full width at half-maximum (fwhm) height Gaussian apodization. The ^{29}Si fwhm values stated herein were estimated separately in the absence of signal apodization.

2.4. Molecular Dynamics Simulations. The classical MD simulations[48] emulating a melt-quench procedure employed the DLPOLY3 package,[49] and an *NVT* ensemble in a cubic box with periodic boundary conditions. The box-length and number of atoms ranged within 3.33−3.54 nm and 3000−3500, respectively, and were adjusted to match the density and composition of each glass. Each initial structure was generated by randomly distributing the atoms, subject to the constraint of a 0.5 Å minimum distance in any pair. The melt-quench procedure started from a relaxed structure that was equilibrated for 100 ps at the temperature 3500 K, followed by a 10 ps stepwise decrease of 10 K/ps down to 300 K. The structure was then allowed to equilibrate during 200 ps, of which the trajectory during the last 150 ps was used for analysis. This procedure was repeated eight times for each glass composition, only differing in the (random) initial configuration of the atoms, from which all structural data and their uncertainties were derived. For a few compositions, we verified the absence of significant changes in the simulated results when employing a higher starting temperature (6000 K) and a slower quench-rate of 1 K/ps.

The interatomic potential employed in the MD simulations included both long-range Coulombic and short-range Buckingham terms, the latter given by $U(r)=A \exp\{-r/\rho\} - Cr^{-6}$, with the parameters specified in Table 3. The potential was implemented with a cutoff distance of 8 Å and a Coulomb-interaction cutoff of 12 Å. To alleviate a strong short-range interatomic attraction, a modification of the Buckingham potential was implemented according to standard procedures.[50] A partial charge of 1.8e was employed for all atoms (where e is the elementary charge), except for Si (2.4e) and O (−1.2e). The Coulombic interactions were calculated using the smoothed particle mesh Ewald summation[48] with a relative accuracy of 10^{-6}. The simulations employed a 2 fs step velocity

Table 3. Buckingham Potential Parameters^a

pair	A (eV)	ρ (Å)	C (eV Å^6)
O−O	1844.7458	0.343 645	192.58
Al−O	12201.417	0.195 628	31.997
Si−O	13702.905	0.193 817	54.681
Y−O	11019.6	0.224 173	0
Lu−O	6657.09	0.230 36	0

^{a}Parameters A, ρ, and C of the Buckingham potential employed in all MD simulations. Those for the Y−O and Lu−O interatomic pairs were derived by us (as will be described elsewhere), whereas all others were taken from Du et al.[32,58]

integrator and a Berendsen thermostat with a 1.0 ps relaxation constant.

3. RESULTS

3.1. Dependence of Physical Properties on Glass Composition. Tables 1 and 2 list the measured values of the glass transition temperature, density, molar volume, compactness, and Vickers hardness for each Y and Lu AS glass. While T_g is well-known to increase with the RE^{3+} CFS, but displaying nearly constant values over large compositional ranges within each RE$_2$O$_3$−Al$_2$O$_3$−SiO$_2$ system,[4−8,17,29,34−37,45] most properties of RE AS glasses (e.g., ρ and H_V) additionally exhibit a pronounced dependence on *both* the nature and the content of the RE ion.[3−7,17,29,30,34,37,45,46] This is indeed witnessed by the consistently higher values of T_g and H_V observed from the Lu AS glasses (Table 2) relative to their Y counterparts (Table 1).

Mean T_g-values ($\overline{T}_g$) of 894 °C and 905 °C are observed over the Y and Lu glass series, respectively, both displaying a spread of 3−4 °C within each system. They may be contrasted with our observations from analogous La ($\overline{T}_g$= 877 °C)[45] and Sc ($\overline{T}_g$= 875 °C)[37] specimens, giving the trends $T_g(Sc) \lesssim T_g(La) < T_g(Y) < T_g(Lu)$. Hence, T_g increases significantly as the RE^{3+} CFS enhances, except for anomalously low glass transition temperatures observed for Sc AS glasses,[7,37] considering that Sc^{3+} features the highest CFS among all RE^{3+}.

Both the density and microhardness, on the other hand, depend strongly on the glass compositions within each RE system. This may be verified from Figure 1 that plots ρ and H_V against the molar fraction of RE$_2$O$_3$ [x(RE$_2$O$_3$)] and SiO$_2$ [x(SiO$_2$)] of the glass, respectively. Naturally, the density of the RE AS glass depends linearly on its constituent of highest mass.[4−7] The Vickers hardness, however, exhibits a more complex dependence on the sample composition (Figure 1b). The H_V-values were fitted to several compositional variables, where two parameters were generally needed to achieve good agreements. The microhardness of the Y−Al−Si−O glasses correlates well with x(Y$_2$O$_3$) alone (correlation coefficient R^2 = 0.96), in accordance with recent observations from Sc AS glasses.[37] The H_V-values of the Lu AS glasses give a decent fit to x(SiO$_2$) (R^2 = 0.90; see Figure 1b) that improves slightly by also including x(Lu$_2$O$_3$) (R^2 = 0.93; data not shown), analogously to our findings from the La$_2$O$_3$−Al$_2$O$_3$−SiO$_2$ system.[45] The somewhat different property/composition relations observed between RE AS glasses based on the pairs {Y^{3+}, Sc^{3+}} relative to the lanthanides {La^{3+}, Lu^{3+}} may derive from their distinct electronic configurations.

3.2. ^{29}Si NMR. Figure 2 shows the ^{29}Si MAS NMR spectra recorded from the Lu and Y AS glasses. Each spectrum reveals exclusively Si$^{[4]}$ coordinations and displays a slightly asymmetric Gaussian peak-shape, centered in the range between
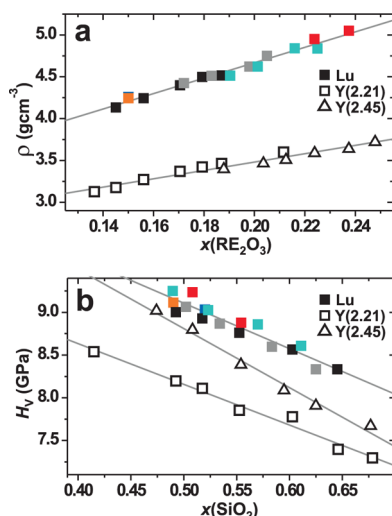
Figure 1. Values of the (a) density and (b) Vickers hardness plotted against the molar fraction of RE_2O_3 and SiO_2, respectively, of the RE−Al−Si−O (RE = Y, Lu) AS glasses. Open and solid symbols represent data from Y and Lu glasses, respectively, grouped in series of constant r-values [see eq (1)] with r given within parentheses; squares (2.21) and triangles (2.45) for Y; solid squares of the following color for Lu: orange (2.07); blue (2.10); black (2.21); gray (2.30); cyan (2.37); red (2.45). Straight lines represent best-fit results and all experimental uncertainties are within each symbol-size.

−90 ppm and −80 ppm and tailing toward lower shifts. The degree of asymmetry may be appreciated from Tables 1 and 2 that list the ^{29}Si NMR peak maximum (δ_{max}) together with the corresponding center-of-gravity shift (δ_{CG}): the latter are consistently displaced by 1.5−2.0 ppm toward lower shifts relative to δ_{max}.

The ^{29}Si NMR peak-maximum moves toward less negative chemical shifts for increases in either the Al content (n_{Al}/n_{Si} ratio) of the glass or its network polymerization (r-value);[7,29,33] the latter dependence is evidenced by Figure S2 of the Supporting Information. When both r and n_{Al}/n_{Si} remain constant, no striking differences are observed in either the δ_{CG} or δ_{max} values between the Y and Lu AS samples: the ^{29}Si NMR

peaks of the Lu−Al−Si−O glasses are slightly less shielded and somewhat broader compared to their Y analogues (Tables 1 and 2). These trends are conveyed by Figure 3a that plots δ_{CG} against x_{Al} for the Lu and Y glasses associated with $r = 2.21$, together with the results from two more depolymerized networks ($r = 2.37$ for Lu and $r = 2.45$ for Y), as well as the corresponding data reported by Iftekhar et al.[29] from La−Al−Si−O glasses featuring $r = 2.21$. Throughout, the δ_{CG}-values only depend weakly on the identity of the RE^{3+} ion, whereas they are much more sensitive to variations of the glass composition.

By a "split network analysis",[51] the set of coexisting $\{Q_{Si}^n(mAl)\}$ tetrahedra may be approximated by a network built from a single fictive tetrahedral species, $Q_{Si}^{\bar{n}}(\bar{m}Al)$, whose values $\bar{n}$ and $\bar{m}$ dictate its ^{29}Si shift δ_{CG};[7,29] a change of $\bar{n} \to \bar{n} - 1$ or $\bar{m} \to \bar{m} + 1$ leads to roughly 8−12 and 4−6 ppm increased δ_{CG}-value, respectively.[19−21,23,27] The ^{29}SiO$_4$ chemical shift from an aluminosilicate also depends on the intertetrahedral Si−O−T (T = Si, Al) bond angles.[20−23] However, the weak dependence of δ_{CG} on the nature of the RE^{3+} ion (Figure 3) for a *fixed* glass composition suggests very similar (i) Si−O−T bond-angle distributions, and (ii) average numbers of BO atoms ($\bar{n}$) and AlO$_4$ neighbors ($\bar{m}$) among the various RE−Al−Si−O (RE = La, Y, Lu) structures. Feature i is verified by our MD simulations [see the Supporting Information]. Although property ii cannot be unambiguously ascertained by our data, the ^{29}Si NMR peak-displacements on changes in the glass composition most likely derive from an increased $\bar{m}$-value when the n_{Al}/n_{Si} ratio grows, and/or a decrease in $\bar{n}$ as r increases.

The fwhm of the ^{29}Si NMR peak reflects the glass network *disorder* and depends strongly both on the glass composition and on the RE^{3+} CFS.[7,8,22,29,33,37] The ^{29}Si fwhm increases for enhancing modifier CFS.[7,8,20−23,27,29] However, since Y^{3+} and Lu^{3+} display very similar ionic radii and average coordination numbers for a given glass composition (verified in section 3.4.3), the slightly smaller Lu^{3+} ion only provides $\approx$1−1.5 ppm broader NMR peak-widths compared to its Y counterparts (see Tables 1 and 2). The fwhm values of the ^{29}Si NMR peaks are plotted versus x_{Al} in Figure 3b. As for the set of $\{\delta_{CG}\}$ values, the NMR peak narrows as either the Al content or r-value of the glass increases. The latter implies a lowering in $\bar{n}$, and the
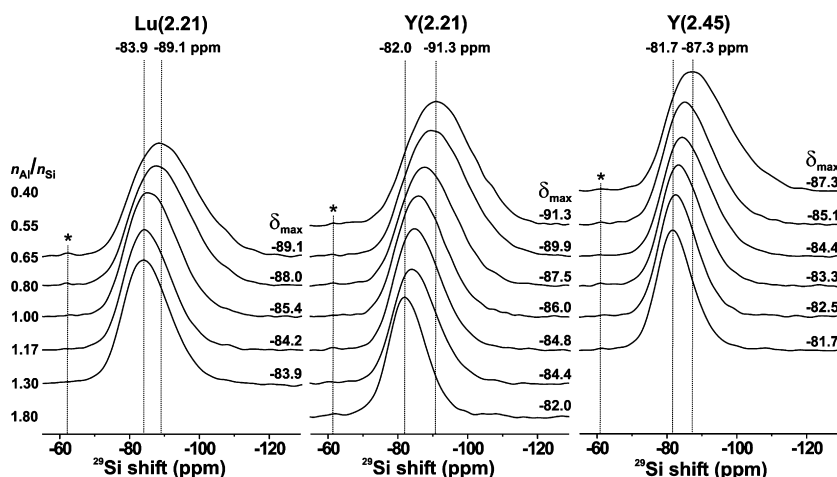

Figure 2. ^{29}Si MAS NMR spectra for Lu (left panel) and Y (mid and right panels), recorded at 9.4 T and grouped according to constant r-value (specified within parentheses) and the molar ratio n_{Al}/n_{Si} increasing from top to bottom. The peak maximum (in ppm) is specified at the right portion of each NMR spectrum. The minor peak around −62 ppm marked by an asterisk stems from minute amounts of crystalline orthosilicate impurities.
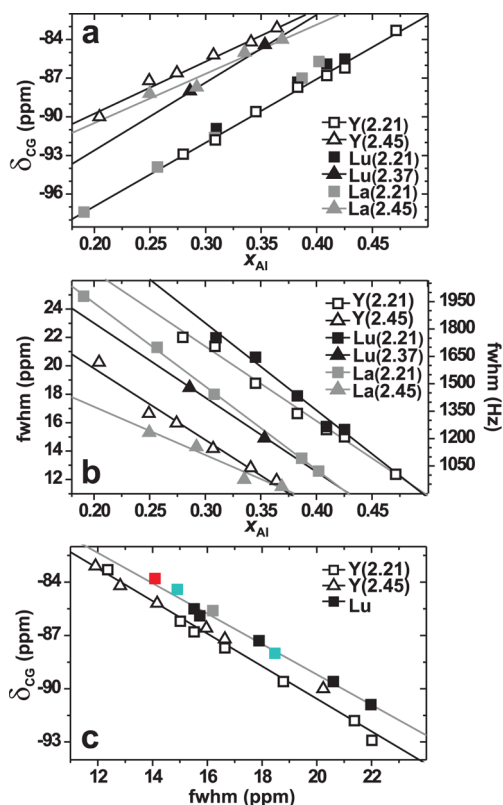
Figure 3. (a) Center-of-gravity ^{29}Si chemical shift (δ_{CG}) and (b) fwhm plotted against the molar fraction of Al in the RE AS glass, with RE corresponding to Y (open symbols), Lu (black solid symbols), and La (gray solid symbols; data reproduced from Iftekhar et al. [29]). The results are grouped according to glasses of constant r-value, as specified by the legends. Note the very similar δ_{CG}-values observed among the distinct RE glasses exhibiting equal r-values, particularly those with r = 2.21. (c) δ_{CG} plotted versus the fwhm of each ^{29}Si NMR peak, with symbol identifications as in Figure 1. All experimental uncertainties in parts a−c are within each symbol-size, and straight lines represent best-fit results.

apparent network ordering likely stems from a concurrent reduction in the distribution of m-values in the set $\{Q^n_{Si}(mAl)\}$, which due to the bound $m \leq n$ naturally narrows as $\bar{n}$ decreases. As shown in the Supporting Information, only minor changes are observed in the distribution *widths* of the Si−O−T bond-angles (that contribute to the NMR peak-width associated with each $Q^n_{Si}(mAl)$ group) for variations in either the Al content or the r-value of the glass network. Hence, our present MD simulations corroborate previous suggestions[7,37] that alterations of both the ^{29}Si δ_{CG} and fwhm values stem predominantly from changes in the n and m parameters among the $\{Q^n_{Si}(mAl)\}$ tetrahedra as the glass composition varies. Furthermore, Figure 3c evidences a good correlation between the sets of δ_{CG} and fwhm data within each series of Lu and Y glasses.

3.3. ^{27}Al NMR. Figure 4 displays ^{27}Al MAS NMR spectra zoomed around the central transition (CT) resonance-region and recorded from the series of RE−Al−Si−O glasses for RE = Y (left panel) and RE = Lu (mid and right panels). Three main ^{27}Al CT resonances ≈53 ppm, ≈30 ppm, and ≈0 ppm are observed throughout, evidencing the coexistence of AlO₄, AlO₅, and AlO₆ polyhedra, respectively.[7,8,20−24,26−30,33,35−37] Analogously to ^{29}Si, the ^{27}AlO₄ resonances move toward higher shifts for increasing Al content of the glass, as also reported previously for the La, Y, and Sc AS systems.[7,24,30,33,35−37] For
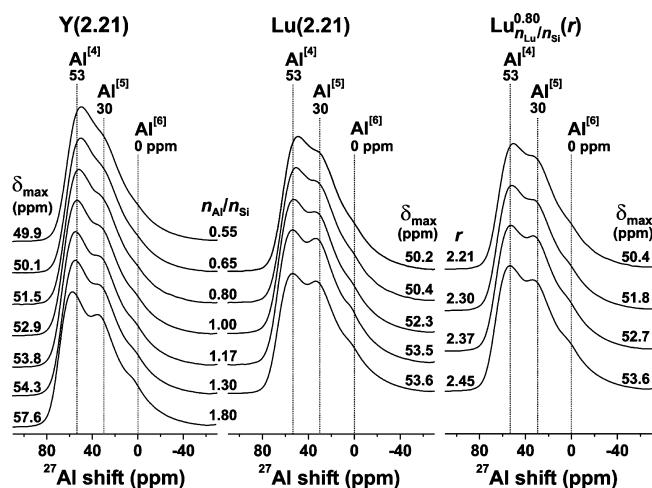

Figure 4. ^{27}Al MAS NMR spectra obtained at 14.1 T from Y−Al−Si−O glasses (left panel) and Lu−Al−Si−O glasses (mid and right panels) that are grouped according to constant r-value of 2.21 (left and mid panels) for increasing n_{Al}/n_{Si}-ratio from top to bottom, while the right panel shows results from Lu AS glasses with constant $n_{Al}/n_{Si} = 0.80$ and increasing r-value. Numbers given at the bottom part of the spectra represent peak maxima of the ^{27}AlO₄ NMR signals.

the case of Y, the shift-elevation amounts to ≈7 ppm across the span of n_{Al}/n_{Si} ratios. This observation also applies to the glass-branch associated with r = 2.45 (Figure S4 of the Supporting Information), as well as for the Lu₂O₃−Al₂O₃−SiO₂ system (Figure 4) that display similar differences in the NMR peak-maxima of around ≈3−4 ppm when either the n_{Al}/n_{Si}-ratio enhances from 0.65 and 1.30 (mid panel) or as the r-value increases from 2.21 to 2.45 at a constant ratio $n_{Al}/n_{Si} = 0.80$ (right panel).

To gain quantitative insight into the compositional dependence of the ^{27}Al NMR parameters and the relative populations of the AlO$_p$ (p = 4, 5, 6) polyhedra, the ^{27}Al MAS NMR spectra were deconvoluted, as described in the Supporting Information. For each Al$^{[p]}$ coordination, the extracted parameters include its fractional population ($x^{[p]}_{Al}$), *average* isotropic ^{27}Al chemical shift ($\delta^{[p]}_{iso}$) and quadrupolar product $C^{[p]}_{Q\eta} = C^{[p]}_Q(1 + \eta^2/3)^{1/2}$, where $C^{[p]}_Q$ and η denote the quadrupolar coupling constant and asymmetry parameter of the electric field gradient tensor, respectively.[22] The best-fit parameters are listed in Tables 4 and 5 for the Y and Lu AS glasses, respectively. In accordance with previous observations from RE₂O₃−Al₂O₃−SiO₂ glasses,[7,24,30,36,37] the ^{27}Al quadrupolar products of the present samples decrease for increasing Al coordination number: $C^{[4]}_{Q\eta} > C^{[5]}_{Q\eta} > C^{[6]}_{Q\eta}$. The $C^{[4]}_{Q\eta}$ values (10.5−10.9 MHz) are similar for both RE systems. They agree well with those reported from Y−Al−Si−O glasses by Florian et al.,[36] as do the mean isotropic chemical shifts $\{\delta^{[4]}_{iso}, \delta^{[5]}_{iso}, \delta^{[6]}_{iso}\}$ ≈ {63−70, 36−40, 6−10} ppm, although the present compositions generally display lower n_{Al}/n_Y and higher n_{Al}/n_{Si} ratios compared with those of Florian et al.[36] The Lu AS glasses reveal slightly higher (by 0.5−0.7 MHz) $C^{[5]}_{Q\eta}$ and $C^{[6]}_{Q\eta}$ values relative to their Y counterparts.

Figure 5 displays the variations of $\delta^{[4]}_{iso}$ and $\delta^{[5]}_{iso}$ against x_{Si} for each AS glass. Both the ^{27}AlO₄ and ^{27}AlO₅ isotropic chemical shifts increase linearly for decreasing x_{Si}, with nearly identical slopes found for both RE systems. The $\delta^{[5]}_{iso}$-values change marginally and depend solely on x_{Si}, whereas the ^{27}AlO₄ chemical shift additionally carries a weak dependence on the

Table 4. Results of MD Simulations and ^{27}Al NMR on the Y–Al–Si–O System^a

glass	$\bar{Z}_Y$	$x_O^{[0]}$	$x_O^{[1]}$	$x_O^{[2]}$	$x_O^{[3]}$	{$\delta_{iso}^{[4]}$; $\delta_{iso}^{[5]}$; $\delta_{iso}^{[6]}$} (ppm)	{$C_{Q\eta}^{[4]}$; $C_{Q\eta}^{[5]}$; $C_{Q\eta}^{[6]}$} (MHz)	$x_{Al}^{[4]}$	$x_{Al}^{[5]}$	$x_{Al}^{[6]}$	$\bar{Z}_{Al}$
$Y^{0.55}_{0.40}(2.21)$	5.89	0.007	0.218	0.711	0.064	62.6; 35.7; 6.8	10.84; 9.54; 7.80	0.830(0.871)	0.153(0.123)	0.017(0.006)	4.19(4.13)
$Y^{0.65}_{0.45}(2.21)$	5.95	0.009	0.225	0.689	0.077	62.7; 35.8; 6.3	10.73; 9.56; 7.77	0.822(0.855)	0.160(0.138)	0.018(0.007)	4.20(4.15)
$Y^{0.80}_{0.52}(2.21)$	6.06	0.007	0.226	0.678	0.089	64.1; 36.2; 7.1	10.73; 9.62; 7.83	0.796(0.823)	0.179(0.165)	0.025(0.012)	4.23(4.19)
$Y^{1.00}_{0.62}(2.21)$	6.16	0.010	0.227	0.659	0.104	65.5; 37.0; 7.4	10.72; 9.72; 7.83	0.776(0.772)	0.195(0.210)	0.029(0.018)	4.25(4.25)
$Y^{1.17}_{0.69}(2.21)$	6.20	0.011	0.231	0.636	0.122	66.4; 37.3; 7.4	10.70; 9.47; 7.80	0.762(0.762)	0.202(0.217)	0.036(0.021)	4.27(4.26)
$Y^{1.30}_{0.76}(2.21)$	6.25	0.010	0.229	0.630	0.131	66.8; 37.4; 7.6	10.70; 9.56; 7.83	0.755(0.739)	0.208(0.238)	0.037(0.023)	4.28(4.28)
$Y^{1.80}_{1.02}(2.21)$	6.35	0.015	0.234	0.589	0.162	69.7; 39.6; 9.5	10.64; 9.56; 7.83	0.723(0.670)	0.232(0.295)	0.045(0.035)	4.32(4.37)
$Y^{0.40}_{0.56}(2.45)$	6.07	0.020	0.339	0.606	0.035	62.8; 35.8; 6.4	10.51; 9.62; 7.81	0.816(0.829)	0.159(0.160)	0.025(0.011)	4.21(4.18)
$Y^{0.55}_{0.65}(2.45)$	6.11	0.022	0.338	0.594	0.046	65.5; 36.5; 6.8	10.72; 9.59; 7.83	0.800(0.802)	0.169(0.183)	0.031(0.015)	4.24(4.21)
$Y^{0.65}_{0.72}(2.45)$	6.16	0.023	0.336	0.592	0.049	65.4; 36.4; 6.8	10.69; 9.62; 7.83	0.800(0.796)	0.171(0.189)	0.029(0.015)	4.23(4.22)
$Y^{0.80}_{0.81}(2.45)$	6.24	0.023	0.337	0.575	0.065	66.7; 37.3; 7.8	10.67; 9.60; 7.78	0.777(0.742)	0.187(0.233)	0.036(0.025)	4.26(4.28)
$Y^{1.00}_{0.94}(2.45)$	6.30	0.025	0.336	0.563	0.076	68.4; 38.4; 8.6	10.66; 9.62; 7.83	0.746(0.728)	0.210(0.245)	0.044(0.027)	4.30(4.30)
$Y^{1.17}_{1.05}(2.45)$	6.38	0.027	0.323	0.560	0.090	69.2; 38.9; 9.2	10.63; 9.62; 7.83	0.749(0.674)	0.208(0.294)	0.043(0.032)	4.29(4.36)

^{a}Average Y coordination number $\bar{Z}_Y$ and fractional population $x_O^{[p]}$ of O$^{[p]}$ (p = 0, 1, 2, 3) coordinations, as obtained from MD simulations. The best-fit average ^{27}Al isotropic chemical shift, $\delta_{iso}^{[p]}$ ($\pm$0.3 ppm), and quadrupolar product $C_{Q\eta}^{[p]}$ ($\pm$0.2 MHz) of the AlO$_p$ polyhedra (whose respective uncertainties are given within parentheses) were obtained by deconvolution of the experimental ^{27}Al MAS NMR spectra, as described in the Supporting Information. The rightmost columns list $x_{Al}^{[p]}$ and mean Al coordination numbers ($\bar{Z}_{Al}$) derived from NMR and MD simulations (the latter within parentheses). The $x_{Al}^{[p]}$ values in each data set are associated with uncertainties of 0.015 (NMR) and 0.02 (MD).

Table 5. Results of MD Simulations and ^{27}Al NMR on the Lu–Al–Si–O System^a

glass	$\bar{Z}_{Lu}$	$x_O^{[0]}$	$x_O^{[1]}$	$x_O^{[2]}$	$x_O^{[3]}$	{$\delta_{iso}^{[4]}$; $\delta_{iso}^{[5]}$; $\delta_{iso}^{[6]}$} (ppm)	{$C_{Q\eta}^{[4]}$; $C_{Q\eta}^{[5]}$; $C_{Q\eta}^{[6]}$} (MHz)	$x_{Al}^{[4]}$	$x_{Al}^{[5]}$	$x_{Al}^{[6]}$	$\bar{Z}_{Al}$
$Lu^{1.47}_{0.61}(2.07)$	5.71	0.007	0.170	0.635	0.188	66.4; 38.4; 8.7	10.91; 10.18; 8.42	0.697(0.737)	0.268(0.240)	0.035(0.023)	4.34(4.29)
$Lu^{1.27}_{0.58}(2.10)$	5.72	0.008	0.176	0.647	0.169	66.5; 38.4; 8.5	10.88; 10.18; 8.36	0.701(0.730)	0.264(0.248)	0.035(0.022)	4.33(4.29)
$Lu^{0.65}_{0.45}(2.21)$	5.53	0.009	0.223	0.684	0.084	63.8; 36.9; 7.0	10.85; 10.29; 8.48	0.754(0.811)	0.225(0.179)	0.021(0.010)	4.27(4.20)
$Lu^{0.80}_{0.52}(2.21)$	5.57	0.011	0.223	0.669	0.097	64.0; 36.8; 7.3	10.84; 10.26; 8.44	0.738(0.799)	0.233(0.188)	0.029(0.013)	4.29(4.21)
$Lu^{1.00}_{0.62}(2.21)$	5.66	0.013	0.230	0.642	0.115	65.5; 37.6; 7.7	10.70; 10.29; 8.36	0.718(0.781)	0.250(0.203)	0.032(0.016)	4.31(4.24)
$Lu^{1.17}_{0.69}(2.21)$	5.71	0.014	0.230	0.626	0.130	66.7; 38.4; 8.1	10.79; 10.27; 8.38	0.693(0.761)	0.270(0.220)	0.037(0.019)	4.34(4.26)
$Lu^{1.30}_{0.76}(2.21)$	5.67	0.014	0.233	0.622	0.131	66.8; 38.5; 8.7	10.82; 10.27; 8.48	0.690(0.768)	0.271(0.213)	0.039(0.019)	4.35(4.25)
$Lu^{0.65}_{0.55}(2.30)$	5.60	0.016	0.267	0.643	0.074	63.5; 36.5; 7.1	10.81; 10.26; 8.48	0.743(0.794)	0.226(0.191)	0.031(0.015)	4.29(4.22)
$Lu^{0.80}_{0.63}(2.30)$	5.63	0.017	0.265	0.639	0.079	64.9; 37.3; 6.6	10.73; 10.23; 8.35	0.726(0.809)	0.242(0.177)	0.032(0.014)	4.31(4.21)
$Lu^{1.00}_{0.74}(2.30)$	5.65	0.021	0.271	0.612	0.096	66.7; 38.5; 9.0	10.75; 10.24; 8.35	0.705(0.789)	0.255(0.198)	0.040(0.013)	4.34(4.22)
$Lu^{1.17}_{0.82}(2.30)$	5.75	0.019	0.270	0.599	0.112	67.7; 39.2; 9.0	10.81; 10.27; 8.36	0.691(0.749)	0.269(0.225)	0.040(0.026)	4.35(4.28)
$Lu^{0.65}_{0.62}(2.37)$	5.53	0.021	0.299	0.622	0.058	65.2; 37.6; 7.6	10.82; 10.15; 8.48	0.730(0.836)	0.234(0.156)	0.036(0.008)	4.31(4.17)
$Lu^{0.80}_{0.71}(2.37)$	5.59	0.023	0.299	0.606	0.072	65.9; 37.7; 8.0	10.75; 10.12; 8.50	0.713(0.820)	0.249(0.165)	0.038(0.015)	4.33(4.19)
$Lu^{1.00}_{0.83}(2.37)$	5.72	0.025	0.299	0.585	0.091	66.8; 38.2; 8.9	10.85; 10.18; 8.53	0.711(0.748)	0.247(0.231)	0.042(0.021)	4.33(4.27)
$Lu^{1.17}_{0.92}(2.37)$	5.69	0.025	0.303	0.576	0.096	67.9; 39.1; 9.4	10.88; 10.17; 8.41	0.688(0.776)	0.269(0.208)	0.043(0.016)	4.36(4.24)
$Lu^{0.80}_{0.81}(2.45)$	5.74	0.028	0.333	0.567	0.072	66.6; 37.9; 8.4	10.90; 10.27; 8.51	0.717(0.744)	0.248(0.233)	0.035(0.023)	4.32(4.28)
$Lu^{1.00}_{0.94}(2.45)$	5.79	0.030	0.330	0.561	0.079	67.5; 38.5; 9.6	10.82; 10.26; 8.48	0.698(0.737)	0.260(0.239)	0.042(0.024)	4.34(4.28)

^{a}The content is analogous to Table 4.

glass network connectivity: $\delta_{iso}^{[4]}$ deshields slightly for increasing r-value of the glass. This trend is most transparent from the Y-bearing samples, whose $\delta_{iso}^{[4]}$-values split into two branches, with up to 3 ppm higher shifts observed from those associated with r = 2.45 for a constant n_{Al}/n_{Si} ratio. This suggests that a minor portion of the total NBO population is located at the AlO$_4$ tetrahedra, in agreement with similar observations from Ca aluminate and low-silica Ca AS glasses,[28] and corroborated further by our MD simulations (section 4.1). The Al$^{[4]}$–NBO contacts induce a slight ^{27}Al$^{[4]}$ deshielding for increasing r, besides that stemming from the Q$_{Al}^n$(mSi)→Q$_{Al}^n$([m−1]Si) conversions and accompanying elevated number of Al$^{[4]}$–O–Al$^{[p]}$ bonds[20,22] for decreasing Si content of the glass network.

3.4. MD Simulations. MD simulations were carried out both for assisting the establishment of structure-composition relations and for probing some structural details not accessible by our NMR experimentation, such as the speciations of RE and O coordinations and the distributions of intertetrahedral bond angles among the AlO$_4$/SiO$_4$ network groups. The Supporting Information highlights several consistency checks regarding the MD-derived short-range glass structures.

3.4.1. Al Speciations: Comparison between NMR and MD Results. The mean Al^{3+} coordination numbers ($\bar{Z}_{Al}$) and the sets of fractional populations {$x_{Al}^{[p]}$} of the {Al$^{[p]}$} coordinations obtained by solid-state NMR and MD simulations are listed in Tables 4 and 5 for the Y and Lu glasses, respectively. We initially focus on examining the experimental $x_{Al}^{[p]}$-values (p = 4,
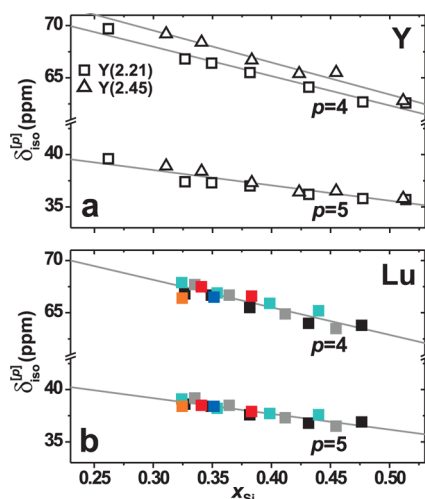
Figure 5. Isotropic chemical shifts ($\delta_{iso}^{[p]}$) of $^{27}AlO_p$ (p = 4, 5) polyhedra plotted against x_{Si} of the RE AS glass for RE representing (a) Y and (b) Lu. See Figure 1 for color identifications. Gray lines illustrate best-fit results.

5) that are plotted against x_{Si} of each Y and Lu bearing glass in Figure 6(a, b). As expected from the ^{27}Al MAS NMR spectra (Figure 4), the AlO_4 tetrahedra dominate the $Al^{[p]}$ speciation, amounting to 72−83% for the Y-bearing specimens, and somewhat lower (69−75%) for those based on Lu, whereas the AlO_6 groups stay below 5% throughout (Tables 4 and 5). In accordance with the higher CFS of Lu^{3+}, these AS glasses feature consistently higher contributions from $Al^{[5]}$ coordinations (23−27%) relative to those of Y (15−23%). We conclude that the $Al^{[p]}$ speciation is dictated primarily by x_{Si}, on which it roughly depends linearly, as also reported by Florian et al.[36] for La and Y AS glasses.

Overall, the modeled average Al coordination numbers display excellent agreement with the experimental results (Tables 4 and 5): they typically agree within <1% discrepancy for the Y AS glasses, whereas for the Lu specimens the simulations slightly underestimate $\bar{Z}_{Al}$ (by $\lesssim$3% relative).

Further, the trends of the simulated $x_{Al}^{[p]}$ populations display good *semiquantitative* agreement with the experimental data. The latter exhibit slightly higher $x_{Al}^{[6]}$-values, but both methods accord excellently within their roughly equal uncertainties. Parts c and d of Figure 6 plot both the experimental and simulated $x_{Al}^{[5]}$ values against x_{Si}. The modeled AlO_4 and AlO_5 populations reproduce the experimentally observed linear trend against x_{Si}; while the calculated $x_{Al}^{[5]}$ values of the Lu AS glasses are scattered and somewhat lower than their experimental counterparts, their relative growth against x_{Si} matches well those of the experiments. For the Y-based glasses, the simulated $x_{Al}^{[5]}$ values are lower (higher) than the corresponding experimental ones for high (low) Si contents, amounting to a larger dynamic range obtained from the MD simulations compared with the experiments. However, due to the much faster quench-rate employed in the simulations compared with that for the glass preparation, one expects *overestimated* MD-derived $x_{Al}^{[5]}$ and $x_{Al}^{[6]}$ values relative to the experimental counterparts (vide infra), which was only observed for the AlO_5 populations of a few Y−Al−Si−O glasses. We have currently no explanation for these findings. Nevertheless, these caveats must be considered relatively minor and our assessments clearly validate the semiquantitative predicting power of the MD data.

3.4.2. O Coordinations. The fractional population $x_O^{[p]}$ of each $O^{[p]}$ coordination was derived for all glass structures. We only consider the coordinations to Al and Si. Tables 4 and 5 list the total O speciation, represented by $O^{[0]}$, $O^{[1]}$, $O^{[2]}$, and $O^{[3]}$ coordinations and revealing that the $x_O^{[1]}$-values remain essentially constant within each r-branch of both the Y and Lu AS systems, as expected. They amount to ≈0.22 and ≈0.33 for r = 2.21 and r = 2.45, respectively, whereas the relative fractions of $O^{[2]}$ and $O^{[3]}$ coordinations mutually exchange as the glass composition varies.

$O^{[3]}$ species are often called "oxygen triclusters", as they involve an oxygen atom shared by three TO_4 (T = Si, Al) groups;[40] here we refer to a tricluster as any constellation of polyhedra binding to the $O^{[3]}$ species. They are known to exist in several well-ordered aluminate (e.g., grossite; $CaAl_4O_7$) and aluminosilicate (e.g., mullite) structures, but their presence in
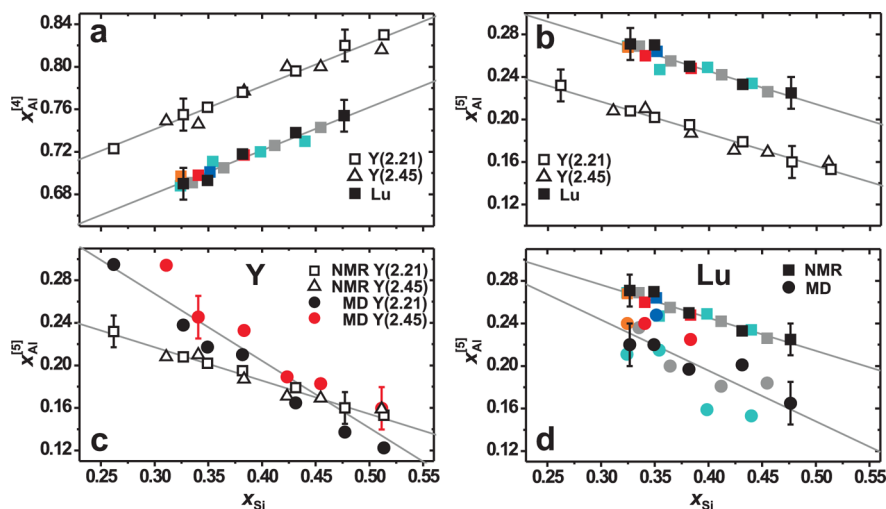

Figure 6. (a, b) ^{27}Al NMR-derived fractional populations of $^{27}AlO_p$ (p = 4, 5) polyhedra plotted versus x_{Si} for (a) p = 4 and (b) p = 5. See Figure 1 for symbol identifications. (c, d) Comparison of $x_{Al}^{[5]}$-values obtained by NMR (symbols as in parts a, b) and MD simulations (circles) for RE−Al−Si−O glasses, where RE represents (c) Y and (d) Lu. The lines in parts a−d correspond to best-fit results. For visual clarity, the uniform error bars are only indicated at a few data-points.
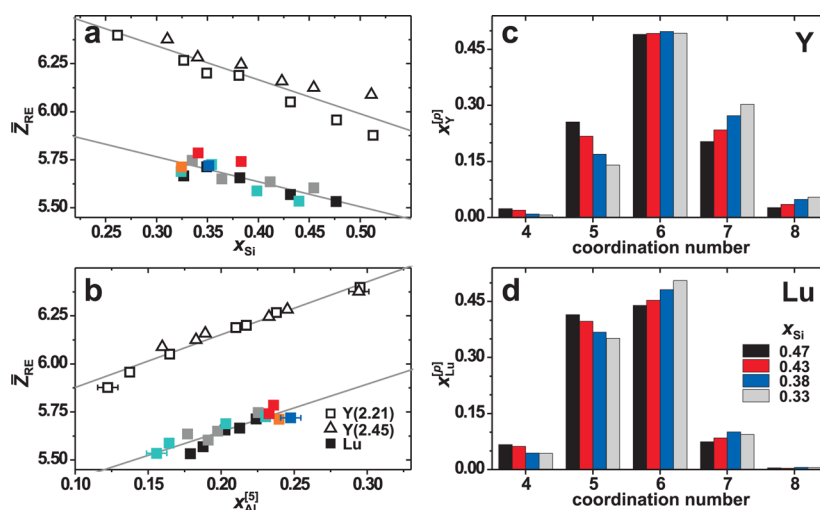
Figure 7. (a, b) MD-derived average RE$^{[p]}$ (RE=Y, Lu) coordination numbers plotted against (a) x_{Si} and (b) $x_{Al}^{[5]}$ of the AS glasses. See Figure 1 for symbol identifications. All vertical error bars are within the size of the symbols, whereas only a few of the uniform horizontal bars are indicated for visual clarity. Lines correspond to best-fit results. (c, d) Fractional populations $x_{RE}^{[p]}$, with RE representing (c) Y and (d) Lu, plotted against the coordination number p.

amorphous phases is debated: O$^{[3]}$ coordinations are frequently observed from MD simulations of aluminosilicate glasses[11,32,43] and has been suggested in several experimental studies,[19,41,42] but have hitherto eluded direct experimental evidence, except for one Ca aluminate glass.[44] Our MD-derived $x_O^{[3]}$ fractions range between 0.04−0.19 (Tables 4 and 5) and correlate primarily with the Al content of the glass. Few Si atoms (typically <10%) coordinate O$^{[3]}$ species that mainly associate with AlO$_5$ polyhedra and to a lesser extent AlO$_4$. Figure S8 of the Supporting Information depicts a typical structural motif involving an O$^{[3]}$ tricluster. The presence of overbonded O atoms signifies a lack of local charge compensation around the Al^{3+} and Si^{4+} cations, as witnessed by the clear trend of O$^{[3]}$ depletion for increasing RE^{3+} content of the glass (and thereby r-value). Indeed, as expected, the Y$_{1.02}^{1.80}$(2.21), Lu$_{0.61}^{1.47}$(2.07), and Lu$_{0.58}^{1.27}$(2.10) structures that feature high n_{Al}/n_{RE} ratios exhibit the largest $x_O^{[3]}$ populations (0.16−0.19).

Another debated O species is "free" O$^{2−}$ ions (O$^{[0]}$), of which there is hitherto no *direct* unambiguous experimental evidence in glasses, although a partially resolved ^{17}O NMR signal from (Ca, Mg) silicate glasses has been attributed to such species,[52] and their presence have sometimes been postulated or estimated indirectly.[7,53−55] 0.7−3.0% O$^{[0]}$ coordinations are observed in our MD-derived structures, in good agreement with a previous MD report on two Y−Al−Si−O compositions,[11] although these small amounts cannot be ruled out to be "artifacts" of the MD simulations. They are signatures of RE^{3+} ion-clustering, i.e., RE−O−RE motifs. Indeed, $x_O^{[0]}$ grows as x_{RE} increases in both the Y−Al−Si−O and Lu−Al−Si−O glass systems (Tables 4 and 5). Slightly higher $x_O^{[0]}$ values are observed from the Lu AS glasses, as expected from the higher CFS of Lu^{3+} compared to Y^{3+}.

3.4.3. Rare-Earth Coordinations. As the glass composition alters within each RE AS system, the average coordination number ($\overline{Z}_{RE}$) of Lu and Y varies between 5.5−5.8 and 5.9−6.4, respectively (Tables 4 and 5). The overall lower $\overline{Z}_{Lu}$-values relative to those of $\overline{Z}_{Y}$ is consistent with the smaller ionic radius of Lu^{3+}. Figure 7a shows that $\overline{Z}_{RE}$ increases roughly linearly for decreasing x_{Si} of the glass, giving correlation coefficients R^2 = 0.84 and R^2 = 0.68 for Y and Lu, respectively. Hence,

compositions associated with low Si contents feature the highest $\overline{Z}_{RE}$-values. Only marginal improvements resulted by attempting two-parameter fits including x_{Si} and another glass-composition variable. Interestingly, $\overline{Z}_{RE}$ correlates strongly with the AlO$_5$ population within each RE system: the MD-derived $\overline{Z}_{RE}$ and $x_{Al}^{[5]}$ data relate linearly (Figure 7b) with correlation coefficients R^2 of 0.96 and 0.81 for Y and Lu, respectively.

Parts c and d of Figure 7 plot the distribution of RE$^{[p]}$ fractional populations for AS glasses with variable Si contents. YO$_6$ and LuO$_6$ polyhedra dominate each respective distribution, but that for Lu^{3+} is strongly skewed toward 5-fold coordinations (with minor Lu$^{[4]}$ contributions of 0.04−0.07), whereas YO$_7$ polyhedra constitute up to ≈30% of the entire Y speciation. Net LuO$_5$ → LuO$_6$ and YO$_5$ → YO$_7$ conversions are observed as x_{Si} decreases for the Lu and Y AS glasses, respectively, whereas the dominating YO$_6$ species remain essentially constant ≈50% throughout the ensemble of Y AS glasses.

4. DISCUSSION

4.1. NBO-Partitioning between SiO$_4$ and AlO$_4$ Groups. The slightly elevated ^{27}AlO$_4$ chemical shifts observed from our NMR data for increasing r-value of the glasses suggests the accommodation of NBO ions also at the AlO$_4$ groups. While other structural factors may be responsible for the ^{27}AlO$_4$ chemical shift-trend, its origin from Al−O$^{[1]}$ bonds is further supported by previously reported ^{29}Si NMR data on La−Al−Si−O glasses,[29] where we inferred a significant element of randomness in the BO/NBO partitioning among the AlO$_4$ and SiO$_4$ tetrahedra. However, in the current absence of *direct* experimental evidence for the presence of NBO ions at AlO$_4$ groups for formally charge-compensated glass compositions, such as the present ones associated with n_{Al}/n_{RE} < 3, MD simulations offer an attractive probe method. The Al$^{[4]}$−NBO and Si−NBO populations within each MD-derived glass network was assessed by counting their respective numbers N_{NBO}^{Al} and N_{NBO}^{Si}. The fraction x_{NBO}^{Al}(sim) = $N_{NBO}^{Al}/(N_{NBO}^{Al} + N_{NBO}^{Si})$ was then compared with the corresponding result of assuming a statistical ("random") distribution of O$^{[1]}$ species among the network tetrahedra; x_{NBO}^{Al}(random) = $n_{Al}^{[4]}/(n_{Al}^{[4]} + $

n_{Si}). Here $n_{Al}^{[4]} = x_{Al}^{[4]} n_{Al}$, with n_{Al} and n_{Si} given by the glass composition, whereas $x_{Al}^{[4]}$ is the MD-derived fraction of AlO$_4$ groups out of the total Al speciation (Tables 4 and 5).

Figure 8 plots the values of x_{NBO}^{Al}(sim) against the fraction of AlO$_4$ tetrahedra in the network for each r-series of the Y and Lu
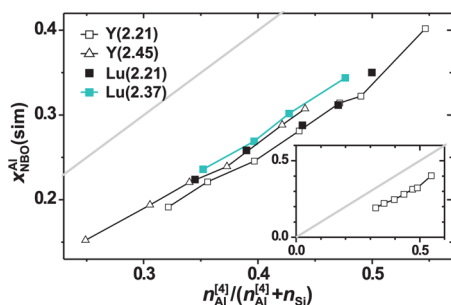

Figure 8. MD-derived fraction of NBO species at the AlO$_4$ groups $[x_{NBO}^{Al}$(sim)$]$ plotted against the fraction of AlO$_4$ in each network of the as-indicated glass series. The gray line of unity slope depicts the results of a random NBO partitioning among the SiO$_4$ and AlO$_4$ tetrahedra, whereas a strict Si–NBO association would result in x_{NBO}^{Al}(sim) $\equiv 0$. The inset graph includes only the Y(2.21) results but conveys more transparently how the simulated data relate to these two limiting scenarios.

AS glasses, together with x_{NBO}^{Al}(random), i.e., the "autocorrelation" line of unity slope. In the limit of the SiO$_4$ moieties accommodating all NBO ions, x_{NBO}^{Al}(sim)$\equiv 0$ would result throughout, in clear contradiction to observations. While the data reveals a clear tendency of Si–NBO association, the NBO distribution is significantly disordered, with the fraction of NBO ions located at Al$^{[4]}$ ranging between 0.15–0.41. The number of Al$^{[4]}$–NBO contacts *overall* grows slightly as the CFS or content of the RE^{3+} ion increases, i.e., the Lu–Al–Si–O glasses exhibit slightly higher amounts of depolymerized Q$_{Al}^{n<4}$(mSi) structural groups relative to their Y–Al–Si–O counterparts, as expected.

Our observed x_{NBO}^{Al}-values are substantially higher than those reported from AS glasses based on lower-CFS cations, such as Ca^{2+}, where significant amounts of Al$^{[4]}$–NBO contacts have only been detected in CaO rich and SiO$_2$ poor compositions up to x(SiO$_2$) $\lesssim 0.20^{31}$ and x(SiO$_2$) $\lesssim 0.45.^{28}$ This underscores the strong bearings of the RE^{3+} CFS on the structural features of RE–Al–Si–O glasses, not only concerning the AlO$_p$ speciation, but also the distribution of O$^{[1]}$ species among the network-forming cations. Apparently, the highly charged RE^{3+} ions may stabilize structural moieties that are energetically (strongly) disfavored in systems incorporating cations of lower charge. Yet, in the current absence of direct experimental evidence, these high x_{NBO}^{Al} fractions should be viewed with caution and further work is required to establish (or possibly disprove) the markedly disordered NBO partitioning among the network-forming cations predicted from our MD simulations.

4.2. Structure–Property Correlations. While numerous studies reveal enhanced H_V values of RE–Al–Si–O–(N) glasses when either the CFS or the content of the RE^{3+} ion increases,$^{4-7,17,34,45,46}$ very few (if any) attempts have been made to establish a *direct* link between H_V and structural parameters. The microhardness of a glass depends on the ion-packing density and the strength of the cation–oxygen bonds,^{5,17,34,46,56} and generally increases together with the network connectivity in silicate glasses.^{56} Yet, Figure 1b verifies

that H_V may *increase* together with the r-value of the glass, which is counterintuitive when considering the glass modifier role of the RE^{3+} cations that leads to network fragmentation. Such observations have hitherto been interpreted as a manifestation of the relatively strong RE–O bonds,^{4,5,7,17,24,34,45,46} typically being much stronger than their counterparts involving M^+ or M^{2+} modifiers. Further, Becher et al. proposed that structural cross-linking effects stemming from the relative high $\bar{Z}_{RE}$-values also contribute toward enhancing H_V.^{17} Our observed concomitant increase in H_V and $\bar{Z}_{RE}$ within each RE AS system (see data in Tables 1, 2, 4 and 5) support this suggestion. Here, however, we highlight an alternative explanation for the H_V-elevation of aluminosilicate oxide (or oxynitride) glasses as the CFS and/or content of the RE^{3+} ions increase. Rather than involving the RE^{3+} ions themselves, it stems from their *indirect* structural influences by increasing the amounts of higher-coordination AlO$_p$ polyhedra, whose cross-linking of the various network fragments likely constitutes the main contribution to the increased microhardness.

Equilibria such as

$$REO_7 + AlO_4 \rightleftharpoons REO_{7-q} + AlO_{4+q}, \qquad q = 1, 2 \tag{3}$$
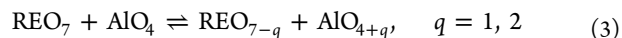
are frequently invoked to rationalize the elevation of $\bar{Z}_{Al}$ for increasing RE^{3+} CFS in AS glasses.^{24,32,36} While they readily explain the higher $\{x_{Al}^{[5]}, x_{Al}^{[6]}\}$ fractions observed herein for the Lu AS glasses relative to their Y analogues, they cannot rationalize the *simultaneous* increase in $\bar{Z}_{Al}$ *and* $\bar{Z}_{RE}$ for growing RE content of the AS glass (see Figure 7). This relationship suggests two concurrent cross-linking, and thereby structure-condensing, contributions: the REO$_p$ polyhedra,^{17} on the one hand, and the AlO$_5$ and AlO$_6$ groups, on the other. While all those populations grow as x_{Si} decreases (i.e., for increasing x_{RE} + x_{Al}), the Al$^{[p]}$–O bond-strengths exceed those of Y$^{[p]}$–O and Lu$^{[p]}$–O, and we attribute the elevation of $\bar{Z}_{Al}$ as *primarily* being responsible for the observed microhardness boost.

These ideas are supported by Figure 9a that evidences an excellent correlation ($R^2 = 0.90$) between H_V and $\bar{Z}_{Al}$ for *all* RE AS glasses. Next, the structure-condensing arguments following the enhanced cross-linking by T–O–Al$^{[p]}$–O–T motifs (where T denotes a network-forming cation and p = 5 or 6) are born out well for the Y AS glasses: Parts b and c of Figure 9 verify linear relationships between H_V and the glass compactness on the one hand, as well as between C and $\bar{Z}_{Al}$, on the other. Owing to the nearly direct relationship between $\bar{Z}_{Al}$ and $x_{Al}^{[5]}$, identical conclusions are reached if instead plotting H_V against $x_{Al}^{[5]}$ (not shown). Further, while H_V also correlates reasonably well with $\bar{Z}_{RE}$ within each Y ($R^2 = 0.83$) and Lu ($R^2 = 0.64$) glass system, $\bar{Z}_{RE}$ does *not* provide a correlation with H_V across the *entire* set of AS glasses. To our knowledge, this constitutes the first directly established link between H_V and a structural parameter in AS glasses: notably, it clarifies the underlying role of the RE^{3+} ions. Similar arguments for the enhanced cross-linking effects from AlO$_5$ and AlO$_6$ (as compared to AlO$_4$) groups has been employed to successfully explain an observed T_g-elevation in Na–Al–P–O glasses.^{57}

Yet, while the $H_V/C/\bar{Z}_{Al}$ interlinking is unambiguously established for the Y glass system, strong relationships between C and H_V, or between C and $\bar{Z}_{Al}$, may not be ascertained for the Lu$_2$O$_3$–Al$_2$O$_3$–SiO$_2$ glasses. The latter data are significantly scattered (Figure 9b,c), where particularly the C-values in part c are unexpectedly low. Most likely, the structure-condensing effect of the AlO$_p$ groups is partially offset by the slightly but consistently lower $\bar{Z}_{Lu}$ values observed compared to those of $\bar{Z}_Y$
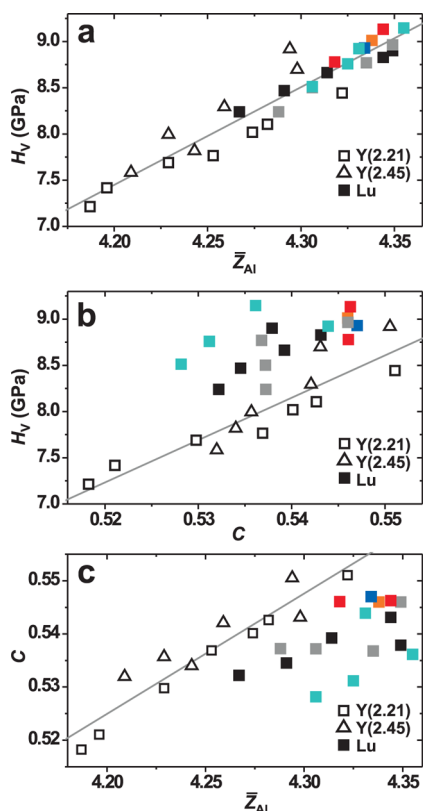
Figure 9. Vickers hardness plotted against the experimental (a) $\overline{Z}_{Al}$ and (b) C data. The gray lines represent best-fit results by considering (a) all samples ($R^2 = 0.90$) and (b) only the set of Y–Al–Si–O glasses ($R^2 = 0.83$). (c) C plotted versus $\overline{Z}_{Al}$, with the gray line representing best-fit results of solely the Y-deriving data ($R^2 = 0.88$). See Figure 1 for symbol identifications.

(see Figure 7). Another caveat of the strong correlation found in Figure 9a is its omission of the Al content of the glass: while the $H_V/\overline{Z}_{Al}$ relationship is nonproblematic when comparing Lu and Y specimens of identical compositions, the variable x_{Al}-values within each individual RE system is not accounted for. However, the results of Figure 9a are *not* simply originating from a concurrent increase in x_{Al} alone, as it correlates very weakly with H_V across both the Y ($R^2 = 0.15$) and Lu ($R^2 = 0.34$) AS systems. Further explorations of other RE AS glass systems are required to establish the generality of the relationship between $\overline{Z}_{Al}$ and H_V observed herein, as well as more precisely defining the links between H_V, C, and the glass composition. The apparently more complex $H_V/\overline{Z}_{Al}$ relationship for the Lu AS glasses is likely related to the absence of a simple correlation between H_V and $x(Lu_2O_3)$ (see section 3.1).

5. CONCLUSIONS

By utilizing ^{29}Si and ^{27}Al solid-state NMR combined with MD simulations, we explored composition/structure/property correlations within the Y_2O_3–Al_2O_3–SiO_2 and Lu_2O_3–Al_2O_3–SiO_2 glass systems, for the latter across its entire glass-forming region, as first reported recently by Iftekhar et al.[7] The glass networks comprise interlinked SiO_4 and AlO_4 tetrahedra. While the NMR-derived $Al^{[p]}$ speciations in both the Y and Lu AS glasses are dominated by $Al^{[4]}$ coordinations and the $x_{Al}^{[6]}$ fractions remain low throughout (<0.05), the amount of AlO_5 groups in the RE AS structures grows linearly for decreasing x_{Si} content and enhances significantly as the CFS

increases from Y^{3+} to Lu^{3+}. The $x_{Al}^{[5]}$-values range between $0.15-0.23$ and $0.23-0.27$ across the set of Y and Lu AS glasses, respectively. The lower span of the latter reflects the narrower range of attainable Lu–Al–Si–O glass compositions. The trends of the MD-derived AlO_p populations accord semi-quantitatively with the NMR results. Our direct comparisons between experimental and simulated $\{AlO_p\}$ speciations represent to our knowledge the first attempt of its kind for a large set of AS glasses. Further, while both the $^{27}AlO_5$ and $^{27}AlO_4$ chemical shifts depend foremost on x_{Si}, particularly the latter increases slightly for growing r-value of the glass. This is tentatively attributed to the enhanced network fragmentation accompanying the increase of NBO ions, where MD simulations reveal that a significant fraction thereof is located at the AlO_4 groups, with the remaining (main) population accommodated at the SiO_4 tetrahedra.

A progressive ^{29}Si NMR peak-narrowing results when either the Al or RE content of the glass increases, as previously observed for Y,[33] La,[29] and Sc[37] AS glasses and suggesting a glass network *ordering*. Because of the absence of significant intertetrahedral bond-angle alterations (as inferred from the MD data), the network-ordering appears to primarily stem from a combination of *topological* (increased network depolymerization by $Q_{Si}^n(mAl) \rightarrow Q_{Si}^{n-1}(mAl)$ conversions) and *chemical* (**Si–O–Si → Si–O–Al** substitutions) effects, rather than geometrical ones.

The MD-derived $O^{[p]}$ speciations comprise nearly constant NBO populations for a constant r-value of the glass but non-negligible amounts of free O^{2-} ions (up to 3%) and significant amounts (4–19%) of $O^{[3]}$ species that predominantly associate with the AlO_p polyhedra. The fraction of $O^{[3]}$ coordinations grows for increasing Al content of the glass (as expected), but diminishes for increasing amount of RE ions.

The RE^{3+} cations mainly exhibit octahedral coordination, with somewhat lower average coordination numbers ($\overline{Z}_{RE}$) observed for the smaller Lu^{3+} ion (5.5–5.8) compared to those of Y^{3+} (5.9–6.4). The $\overline{Z}_{RE}$-values correlate linearly both with the Si content of the sample and its fractional population $x_{Al}^{[5]}$. We found an excellent correlation between H_V and $\overline{Z}_{Al}$ over the entire ensemble of Y and Lu AS glasses. The origin of the enhanced Vickers hardness for an increase in either the RE^{3+} CFS or content stems *indirectly* from their effects on the $\{Al^{[p]}\}$ speciation (where $\overline{Z}_{Al}$ grows both with x_{RE} and the RE^{3+} CFS), which ultimately controls H_V via a structural strengthening accompanying the increased cross-linking and relatively strong $Al^{[5]}$–O–T and $Al^{[6]}$–O–T bonds (where T denotes a network-forming cation) compared to those of $RE^{[p]}$–O. We are currently exploring these relationships in other RE AS glass systems. Our suggested dependence of H_V on $\overline{Z}_{Al}$ is likely also operating in RE–Al–Si–O–N *oxynitride* glass structures, where similar trends of H_V versus the CFS and/or content of the RE^{3+} ions are reported,[17,34,46] but where quantitative Al speciations are hitherto not reported. This is an interesting topic for future investigations.

■ ASSOCIATED CONTENT

⑤ Supporting Information

Additional discussion about ^{29}Si chemical shift trends, deconvolution procedures of the ^{27}Al MAS NMR spectra and MD-derived short-range structural data. Figures: diagrams with glass compositions; additional ^{29}Si NMR spectra and deconvoluted ^{27}Al NMR spectra; plots of MD-derived radial distribution functions and intertetrahedral bond-angle distribu-

tions; an illustration of an oxygen tricluster moiety. This material is available free of charge via the Internet at http://pubs.acs.org.

■ AUTHOR INFORMATION

Corresponding Author
*E-mail: mattias.eden@mmk.su.se.
Notes
The authors declare no competing financial interest.

■ REFERENCES

(1) Makishima, A.; Tamura, Y.; Sakaino, T. *J. Am. Ceram. Soc.* **1978**, *61*, 247.
(2) Makishima, A.; Kobayashi, M.; Shimohria, T.; Nagata, T. *J. Am. Ceram. Soc.* **1982**, *65*, C210.
(3) Hyatt, M. J.; Day, D. E. *J. Am. Ceram. Soc.* **1987**, *70*, C283.
(4) Kohli, J. T.; Shelby, J. E. *Phys. Chem. Glasses* **1991**, *32*, 67.
(5) Kohli, J. T.; Shelby, J. E. *J. Am. Ceram. Soc.* **1991**, *74*, 1031.
(6) Shelby, J. E.; Minton, S. M.; Lord, C. E.; Tuzzolo, M. R. *Phys. Chem. Glasses* **1992**, *33*, 93.
(7) Iftekhar, S.; Grins, J.; Gunawidjaja, P. N.; Edén, M. *J. Am. Ceram. Soc.* **2011**, *94*, 2429.
(8) Marchi, J.; Morais, D. S.; Schneider, J.; Bressiani, J. C.; Bressiani, A. H. A. *J. Non-Cryst. Solids* **2005**, *351*, 863.
(9) Hayward, P. J. *Radioactive Waste Forms for the Future*; North-Holland: Amsterdam, 1988.
(10) Chen, S. D.; Hsieh, J. F.; Tsai, S. C.; Lin, W. Y.; Cheng, K. Y.; Wang, S. J. *Nucl. Med. Commun.* **2001**, *22*, 121.
(11) Christie, J. K.; Tilocca, A. *Chem. Mater.* **2010**, *22*, 3725.
(12) Aasland, S.; McMillan, P. F. *Nature* **1994**, *369*, 633.
(13) Tangeman, J. A.; Phillips, B. L.; Nordine, P. C.; Weber, J. K. R. *J. Phys. Chem. B* **2004**, *108*, 10663.
(14) Du, J.; Benmore, C. J.; Corrales, R.; Hart, R. T.; Weber, J. K. R. *J. Phys.: Condens. Matter* **2009**, *21*, 205102.
(15) Nasikas, N. K.; Sen, S.; Papatheodorou, G. N. *Chem. Mater.* **2011**, *23*, 2860.
(16) Shannon, R. D. *Acta Crystallogr.* **1976**, *32*, 751.
(17) Becher, P. F.; Waters, S. B.; Westmoreland, C. G.; Riester, L. *J. Am. Ceram. Soc.* **2002**, *85*, 897.
(18) Loewenstein, W. *Am. Mineral.* **1954**, *39*, 92.
(19) Engelhardt, G.; Nofz, M.; Forkel, F.; Wishmann, F. G.; Mägi, M.; Samoson, A.; Lippmaa, E. *Phys. Chem. Glasses* **1985**, *26*, 157.
(20) Engelhardt, G.; Michel, D., *High-Resolution Solid-State NMR of silicates and zeolites*; Wiley: Chichester, U.K., 1987.
(21) Oestrike, R.; Yang, W.-H.; Kirkpatrick, R. J.; Hervig, R. L.; Navrotsky, A.; Montez, B. *Geochim. Cosmochim. Acta* **1987**, *51*, 2199.
(22) Edén, M. *Annu. Rep. Prog. Chem., Sect. C: Phys. Chem.* **2012**, *108*, 177.
(23) Murdoch, J. B.; Stebbins, J. F.; Carmichael, I. S. E. *Am. Mineral.* **1985**, *70*, 332.
(24) Schaller, T.; Stebbins, J. F. *J. Phys. Chem. B* **1998**, *102*, 10690.
(25) Lee, S. K.; Stebbins, J. F. *J. Non-Cryst. Solids* **2000**, *270*, 260.
(26) McMillan, P. F.; Petuskey, W. T.; Coté, B.; Massiot, D.; Landron, C.; Coutures, J.-P. *J. Non-Cryst. Solids* **1996**, *195*, 261.

(27) Merzbacher, C. I.; Sheriff, B. L.; Hartmann, J. S.; White, W. B. *J. Non-Cryst. Solids* **1990**, *124*, 194.
(28) Neuville, D. R.; Cormier, L.; Massiot, D. *Chem. Geol.* **2006**, *229*, 173.
(29) Iftekhar, S.; Leonova, E.; Edén, M. *J. Non-Cryst. Solids* **2009**, *355*, 2165.
(30) Leonova, E.; Hakeem, A. S.; Jansson, K.; Stevensson, B.; Shen, Z.; Grins, J.; Esmaeilzadeh, S.; Edén, M. *J. Non-Cryst. Solids* **2008**, *354*, 49.
(31) Allwardt, J. R.; Lee, S. K.; Stebbins, J. F. *Am. Mineral.* **2003**, *88*, 949.
(32) Du, J. *J. Am. Ceram. Soc.* **2009**, *92*, 87.
(33) Kohli, J. T.; Shelby, J. E.; Frye, J. S. *Phys. Chem. Glasses* **1992**, *33*, 73.
(34) Lemercier, H.; Rouxel, T.; Fargeot, D.; Besson, J.-L.; Piriou, B. *J. Non-Cryst. Solids* **1996**, *201*, 128.
(35) Clayden, N. J.; Esposito, S.; Aronne, A.; Pernice, P. *J. Non-Cryst. Solids* **1999**, *258*, 11.
(36) Florian, P.; Sadiki, N.; Massiot, D.; Coutures, J. P. *J. Phys. Chem. B* **2007**, *111*, 9747.
(37) Pahari, B.; Iftekhar, S.; Jaworski, A.; Okhotnikov, K.; Jansson, K.; Stevensson, B.; Grins, J.; Edén, M. *J. Am. Ceram. Soc.* **2012**, *95*, 2545.
(38) Sadiki, N.; Hennet, L.; Florian, P.; Vaills, Y.; Massiot, D.; Coutures, J.-P. *Matér. Tech.* **2010**, *98*, 409.
(39) Pozdnyakova, I.; Sadiki, N.; Hennet, L.; Cristiglio, V.; Bytchkov, A.; Cuello, G. J.; Coutures, J. P.; Price, D. L. *J. Non-Cryst. Solids* **2008**, *354*, 2038.
(40) Lacy, E. D. *Phys. Chem. Glasses* **1963**, *4*, 234.
(41) Stebbins, J. F.; Oglesby, J. V.; Kroeker, S. *Am. Mineral.* **2001**, *86*, 1307.
(42) Schmücker, M.; Schneider, H. *J. Non-Cryst. Solids* **2002**, *311*, 211.
(43) Cormier, L.; Ghaleb, D.; Neuville, D. R.; Delaye, J.-M.; Calas, G. *J. Non-Cryst. Solids* **2003**, *332*, 255.
(44) Iuga, D.; Morais, C.; Gan, Z.; Neuville, D. R.; Cormier, L.; Massiot, D. *J. Am. Chem. Soc.* **2005**, *127*, 11540.
(45) Iftekhar, S.; Grins, J.; Edén, M. *J. Non-Cryst. Solids* **2010**, *356*, 1043.
(46) Ramesh, R.; Nestor, E.; Pomeroy, M. J.; Hampshire, S. *J. Eur. Ceram. Soc.* **1997**, *17*, 1933.
(47) Anstis, G. R.; Chantikul, P.; Lawn, B. R.; Marshall, D. P. *J. Am. Ceram. Soc.* **1981**, *64*, 533.
(48) Allen, M. P.; Tildesley, D. J. *Computer Simulation of Liquids*; Clarendon Press: Oxford, U.K., 1987.
(49) Todorov, I. T.; Smith, W.; Trachenko, K.; Dove, M. T. *J. Mater. Chem.* **2006**, *16*, 1911.
(50) Bakaev, V. A.; Steele, W. A. *J. Chem. Phys.* **1999**, *111*, 9803.
(51) Edén, M. *J. Non-Cryst. Solids* **2011**, *357*, 1595.
(52) Nasikas, N. K.; Edwards, T. G.; Sen, S.; Papatheodorou, G. N. *J. Phys. Chem. B* **2012**, *116*, 2696.
(53) Zhang, P.; Grandinetti, P. J.; Stebbins, J. F. *J. Phys. Chem. B* **1997**, *101*, 4004.
(54) Schaller, T.; Stebbins, J. F.; Wilding, M. C. *J. Non-Cryst. Solids* **1999**, *243*, 146.
(55) Davis, M. C.; Sanders, K. J.; Grandinetti, P. J.; Gaudio, S. J.; Sen, S. *J. Non-Cryst. Solids* **2011**, *357*, 2787.
(56) Smedskjaer, M. M.; Jensen, M.; Yue, Y. *J. Non-Cryst. Solids* **2010**, *356*, 893.
(57) Brow, R. K.; Kirkpatrick, R. J.; Turner, G. L. *J. Am. Ceram. Soc.* **1993**, *76*, 919.
(58) Du, J.; Corrales, L. R. *J. Non-Cryst. Solids* **2007**, *353*, 210.